Electronic Supplementary Information

Two-dimensional iridium-cobalt oxide for high-efficiency acidic oxygen evolution reaction electrocatalysis

Chendi Zhao,[1] Shuangxing Li,[1] Hanzhuo Luo,[1] Jialin Miao,[1] Yujin Ji[*2] and Qi Shao[*1]

[1]College of Chemistry, Chemical Engineering and Materials Science, Soochow University, Suzhou 215123, Jiangsu, China.

[2]Institute of Functional Nano & Soft Materials (FUNSOM), Soochow University, Suzhou 215123, Jiangsu, China.

E-mail: yjji@suda.edu.cn, qshao@suda.edu.cn

Table of Contents

12. **Figure S11.** (a) XRD pattern of IrCoO-3. (b) SEM image of IrCoO-3. (c) TEM image of IrCoO-3. (d) EDS image of IrCoO-3. (e) EDS analysis of IrCoO-3, where the ratio of Co to Ir is 11 : 1.
13. **Figure S12.** (a) XRD pattern of IrCoO-4. (b) SEM image of IrCoO-4. (c) TEM image of IrCoO-4. (d) EDS image of IrCoO-4. (e) EDS analysis of IrCoO-4, where the ratio of Co to Ir is 20 : 1.
14. **Figure S13.** (a) SEM image of IrCoONPS. (b) TEM image of IrCoONPS. (c) XRD pattern of IrCoONPS. (d) EDS image of IrCoONPS. (e) EDS analysis of IrCoONPS, where the ratio of Co to Ir is 4 : 1.
15. **Figure S14.** The IR spectrum of IrCoO-2 and C-Co_3O_4.
16. **Figure S15.** (a) Raman spectra of C-Co_3O_4, IrCoO-2, C-IrO_2 and 1T-IrO_2. (b) Raman image of IrCoO-2.
17. **Figure S16.** (a) O 1s XPS spectra of C-Co_3O_4. (b) O 1s XPS spectra of C-IrO_2.
18. **Figure S17.** Potential calibration of the saturated calomel electrode in 0.5 M H_2SO_4 electrolyte. The calibration was performed in the high purity hydrogen-saturated electrolyte. Two Pt electrodes were used as the working and counter electrodes. Scan rate: 1 mV s^{-1}.
19. **Figure S18.** Tafel plots and corresponding Tafel slopes of IrCoO-2, C-IrO_2 and Ir/C.
20. **Figure S19.** Nyquist diagrams of IrCoO-2, C-IrO_2 and Ir/C. The EIS curves for IrCoO-2, C-IrO_2, and Ir/C at corresponding overpotentials for a current density of 10 mA cm^{-2} are presented respectively for OER in 0.5 M H_2SO_4.
21. **Figure S20.** UPD method used to determine the ECSA. CV curves of (a) IrCoO-2, (b) C-IrO_2 and (c) Ir/C in 0.1 M $HClO_4$ containing 1.0 mM mercury nitrate. The scanning rate was 10 mV s^{-1}.
22. **Figure S21.** (a) Mass activity, (b) SA and (c) TOF of IrCoO-2, C-IrO_2 and Ir/C under different voltage changes.

23. **Figure S22.** CV curves of (a) IrCoO-2, (b) C-IrO_2 and (c) Ir/C with different scan rates in a potential region of 0.94 to 1.06 V *vs.* RHE in 0.5 M H_2SO_4. (f) The corresponding C_{dl} plots of IrCoO-2, C-IrO_2 and Ir/C.
24. **Figure S23.** (a) Polarization curves of C-Co_3O_4 in O_2-saturated 0.5 M H_2SO_4 electrolyte with *i*R-correction, where C-Co_3O_4 deliver an overpotential of 549 mV to achieve the current density of 10 mA cm^{-2}. (b) Tafel plots of C-Co_3O_4. (c) Nyquist plot of C-Co_3O_4. (d) CV curve of C-Co_3O_4 with different scan rates in a potential region of 0.94 to 1.06 V *vs.* RHE in 0.5 M H_2SO_4. (c) The corresponding C_{dl} plots of C-Co_3O_4.
25. **Figure S24.** (a) Polarization curves of IrCoO-1 in O_2-saturated 0.5 M H_2SO_4 electrolyte with *i*R-correction, where IrCoO-1 deliver an overpotential of 254 mV to achieve the current density of 10 mA cm^{-2}. (b) Tafel plots of IrCoO-1 in O_2. (c) Nyquist plot of IrCoO-1. (d) CV curve of IrCoO-1 with different scan rates in a potential region of 0.94 to 1.06 V *vs.* RHE in 0.5 M H_2SO_4. (c) The corresponding C_{dl} plots of IrCoO-1.
26. **Figure S25.** (a) Polarization curves of IrCoO-3 in O_2-saturated 0.5 M H_2SO_4 electrolyte with *i*R-correction, where IrCoO-3 deliver an overpotential of 278 mV to achieve the current density of 10 mA cm^{-2}. (b) Tafel plots of IrCoO-3. (c) Nyquist plot of IrCoO-3. (d) CV curve of IrCoO-3 with different scan rates in a potential region of 0.94 to 1.06 V *vs.* RHE in 0.5 M H_2SO_4. (c) The corresponding C_{dl} plots of IrCoO-3.
27. **Figure S26.** (a) Polarization curves of IrCoO-4 in O_2-saturated 0.5 M H_2SO_4 electrolyte with *i*R-correction, where IrCoO-4 deliver an overpotential of 305 mV to achieve the current density of 10 mA cm^{-2}. (b) Tafel plots of IrCoO-4. (c) Nyquist plot of IrCoO-4. (d) CV curve of IrCoO-4 with

different scan rates in a potential region of 0.94 to 1.06 V *vs.* RHE in 0.5 M H_2SO_4. (c) The corresponding C_{dl} plots of IrCoO-4.

28. **Figure S27.** LSV curves of the samples of IrCoO-2, IrCoO-1, IrCoO-3, IrCoO-4 and IrCoONPS.
29. **Figure S28.** Chronopotentiometry test of IrCoO-2 at the current density of 10 mA cm^{-2} in 0.5 M H_2SO_4.
30. **Figure S29.** (a) XRD pattern, (b) SEM image and (c) TEM image of IrCoO-2 after 106 hours stability test.
31. **Figure S230.** Actual device diagram of PEMWE. The area of Ti mesh is 1×1 cm^2.
32. **Figure S31.** (a) SEM image, (b) TEM image and (c) XRD pattern of IrCoO-2 after 600 hours stability test in PEM device.
33. **Figure S32.** CV curves of IrCoO-2 recorded with and without 0.1 M methanol at the scan rate of 50 mV s^{-1}.
34. **Figure S33.** Comparisons of the energy barriers at the AEM and dual-site atomic oxygen evolution mechanism of IrCoO-2.
35. **Table S1.** The quantity of raw materials input, the iridium-to-cobalt ratio in the catalyst and the catalyst nomenclature.
36. **Table S2.** Overpotential and Tafel slope of IrCoO-1, IrCoO-2, IrCoO-3, IrCoO-4, IrCoONPS, C-IrO2 and Ir/C in 0.5 M H_2SO_4.
37. **Table S3.** Comparison of C_{dl}, mass activity, UPD based ECSA and TOF among the catalysts in acidic OER.
38. **Table S4.** The comparison of the OER performances (overpotential and mass activity) of IrCoO-2 and various reported catalysts.

96

Experimental Procedures

1.1 Chemicals

Iridium (III) acetylacetonate ($C_{10}H_{14}IrO_4$, 98%) was purchased from TCI. (Shanghai, China) Iridium trichloride ($IrCl_3$, 99.9%) was purchased from Alfa Aesar. Commercial iridium oxide (IV) (C-IrO_2, 99%, rutile phase) was purchased from Aladdin. Iridium carbon (Ir/C with Ir of 20 wt%) was purchased from Premitek Co. Cobalt (III) Acetylacetonate ($C_{10}H_{14}CoO_4$, 98%) was purchased from J&K Scientific Ltd. (Beijing, China). Commercial Pt/C (20 wt%) was purchased from Johnson Matthey (JM). Potassium carbonate (K_2CO_3, 99%), isopropanol and sulfuric acid (H_2SO_4, ≥ 96.0%) were obtained by Sinopharm Chemical Reagent Co., Ltd. Nafion solution (5 wt%) and mercury (II) nitrate hydrate ($Hg(NO_3)_2{\cdot}H_2O$, 99.99%) were obtained by Sigma-Aldrich. Carbon support (Vulcan XC-72) was purchased from Vulcan. Other reagents are analytical-reagent-grade and do not need further purification. Double-distilled water was used throughout the experiment. The PEM device was purchased from Shanghai Chuxi Industry Co. Commercial Nafion 212 films were purchased from Energy Chemical Co. High-temperature resistant titanium fiber felt diffusion layer is provided by Kunshan Guangjiayuan Electronic Materials Co, Ltd, with a porosity of 60%-70%.

1.2 Synthesis of IrCoO-x

The synthesis of IrCoO-x nanosheets was conducted within a custom-built high-purity corundum mechanical thermal reactor. Initially, 25 milligrams of $C_{10}H_{14}CoO_4$, 5 milligrams of $C_{10}H_{14}IrO_4$, and 0.8 grams of K_2CO_3 were meticulously ground and subsequently amalgamated in a suitable agate mortar, ensuring complete uniformity. The mixture was subsequently transferred into the mechanical thermoreactor. The reactor was heated from ambient temperature to 850 ℃ at a rate of 5 ℃/min within

a muffle furnace, where it was held for a period of 2 hours. The sample was then cooled to 500 ℃ at a rate of 5 ℃/min before being permitted to cool naturally to room temperature. The product underwent multiple cycles of washing with ultrapure water and drying, yielding IrCoO-2 was obtained. Employing the same method, IrCoO-1, IrCoO-3 and IrCoO-4 were synthesised by adjusting the amount of $C_{10}H_{14}CoO_4$ to 10 mg, 75 mg and 125 mg, respectively. The amount of alkali utilized shall be consistently maintained as a fixed multiple of the quantity of $C_{10}H_{14}CoO_4$. The quantity of $C_{10}H_{14}IrO_4$ remains unchanged. Furthermore, a non-layered iridium-cobalt oxide with an iridium-to-cobalt ratio of 4 : 1 was synthesised via the molten salt method, and was named IrCoONPS (nanoparticles).

1.3 Characterization

Scanning electron microscopy (SEM) images were recorded with Hitachi field emission SEM SU8230 with the accelerating voltage of 15 kV. Low-magnification transmission electron microscopy (TEM) images were collected on a Hitachi HT7700 transmission electron microscope with the accelerating voltage of 120 kV. The crystal nanostructures were analyzed by an X-ray powder diffraction (XRD, X`Pert-Pro MPD diffractometer) equipped with a Cu Kα radiation source (λ = 0.15406 nm). The HRTEM, energy dispersive spectroscopy (EDS) and EDS elemental mapping were achieved by Talos transmission electron microscope with an acceleration voltage of 200 kV. Except for the main material, EDS characterization of all other materials was performed using the SEM SU8230. The atomic resolution HRTEM images were also conducted by Spherical-aberration-corrected TEM (Cs-corrected TEM, FEI Titan Themis Cubed G2300). X-ray photoelectron spectra were collected with an SSI S-Probe XPS Spectrometer. The carbon peak at 284.6 eV was used as a reference for calibration.

1.4 Electrochemical measurements

OER measurements were performed at room temperature, with stirring of the electrolyte solution during the test. Electrochemical measurements were carried out at the CHI660E electrochemical station (Chenhua, Shanghai) using a three-electrode system. The working electrodes were a glassy carbon electrode (GCE) with a diameter of 5 mm and an area of 0.196 cm^2 or carbon paper with an area of 1 cm^2. A saturated calomel electrode (SCE) and a graphite rod were used as the reference and counter electrodes, respectively. To prepare the working electrodes, 1.0 mg of catalyst (The amount of the commercial catalyst used for comparison was 2 mg) was mixed with 400 μL of isopropanol and 5 μL of Nafion solution (5 wt%) for 30 minutes with ultrasonic agitation to form a homogeneous catalyst ink. Then, 10 μL of the ink was cast onto the GCE in an area of 0.1965 cm^2 and left to dry at room temperature. The conversion between the measured potential and the reversible hydrogen electrode (RHE) was calculated by Eq.1:

$$E(vs.RHE) = E(vs.\frac{Hg}{Hg_2Cl_2}) + 0.248\#(1)$$

The ohmic potential drop (*i*R) correction was 95% and R was the ohmic resistance caused by the electrolyte contact resistance of the device. The scan rate was 5 mV s^{-1} for linear sweep voltammetry (LSV) measurements.

The electrochemical double-layer capacitance (C_{dl}) at non-Faradic potential range was obtained by measuring the capacitance of double layer at solid-liquid interface employing CV with different scan rates (5, 10, 15, 20, 25, 30 and 35 mV s^{-1}) ranging from 0.94 and 1.06 V *vs.* RHE. The C_{dl} was calculated by the Eq. 2:

$$C_{dl} = \frac{\Delta j/2}{v} \#(2)$$

where Δj represented the difference between the anodic and cathodic currents (j_a-j_c) at 1.00 V vs. RHE, and v denoted the scan rate.

The electrochemical active surface area (ECSA) was determined through mercury (Hg) underpotential deposition (UPD) measurements. CV curves were tested in 0.1 M $HClO_4$ electrolyte containing 1 mM mercury nitrate with a potential range from 0.25 to 0.8 V *vs.* RHE. The scan rate was 10 mV s^{-1}. ECSA values was calculated through Eqs. 3,4:

$$\mathrm{ECSA} = \frac{Q}{C} \#(3)$$

$$Q = \frac{S_{peak}}{v} \#(4)$$

C is a value of the adsorbed capacity of hydrogen (210 μC cm^{-2}). S_{peak} was the integral area of adsorbed mercury in CV curve, and v was the scan rate of 10 mV s^{-1}.

The turnover frequencies (TOFs) of the electrocatalysts were defined as the produced oxygen by the moles of the active sites per unit time. The TOFs were calculated by Eq.5:

$$\mathrm{TOF}_{\mathrm{UPD/ECSA/BET}} = \frac{\left(1.56 \times 10^{15} \frac{\mathrm{O_2/s}}{\mathrm{cm^2}} \mathrm{per} \frac{\mathrm{mA}}{\mathrm{cm^2}}\right) \times |\mathrm{j}|}{(\text{active sites}) \times \mathrm{A}_{\mathrm{UPD/ECSA/BET}}} \#(5)$$

The average active surface atoms per square centimetre of IrCoO-x was calculated by Eq.6:

$$\text{Active sites}_{(IrCoO-x)} = \frac{0.5 \text{ atom}}{(3.11 \times 3.11)\ \text{Å}^2 \times \sin 60°} = 5.97 \times 10^{14} \frac{\text{atom}}{\text{cm}^2} \#(6)$$

The average active surface atoms per square centimetre of C-IrO_2 were calculated by Eq.7:

$$\text{Active sites}_{(C-IrO_2)} = \frac{2 \text{ atom}}{(4.498 \times 3.154)\ \text{Å}^2 \times \sqrt{2}} = 9.97 \times 10^{14} \frac{\text{atom}}{\text{cm}^2} \#(7)$$

The average active surface atoms per square centimetre of Ir/C were calculated by Eq.8:

$$\text{Active sites}_{(Ir/C)} = \frac{0.5 \text{ atom}}{0.5 \times (\sqrt{2}/2 \times 3.839 \times \sqrt{2}/2 \times 3.839)\ \text{Å}^2 \times \sin 60°} = 15.67 \times 10^{14} \frac{\text{atom}}{\text{cm}^2} \#(8)$$

1.5 Electrochemical measurements in proton exchange membrane water electrolysis.

To construct the membrane electrode assembly (MEA), IrCoO-2 was used as the anode catalyst, and commercial Pt/C (20 wt%) was used as the cathode catalyst. To prepare the anode and cathode ink, catalysts were dispersed into a mixture of isopropanol and Nafion solution (5wt%) with a ratio of 99: 1. After ultrasonic for at least 40 min in a low temperature water bath,

a uniform catalyst ink can be obtained. The ink of the obtained cathode and anode catalysts was uniformly sprayed on the Ti mesh with the active area of 1×1 cm^2 by the spraying equipment.

The proton exchange membrane water electrolysis (PEMWE) performance was tested on battery-testing system (UNI-T UTP1310-‖). The PEMWE was maintained at 80 ℃ during the stability test, using the preheated deionized water as the anode electrolyte. The stability of the PEMWE was evaluated by measuring chronopotentiometry at 1.7 V.

1.6 Computational details

All the DFT calculations are conducted with Vienna ab initio simulation package[1], and spin polarization is taken into account. The ion core and valence electron configurations are initialized with projector augmented wave (PAW) method[2], and the implemented exchange-correlation functional is in the Perdew-Burke-Ernzerhof formulism[3]. For investigating (100) facet of IrCoO-x, the corresponding slab models are built with 4 atomic layers, and the bottom 2 layers are fixed in the structure relaxation. The convergence criteria for the self-consistent loop and geometric relaxation were set to 10^{-4} eV and 0.03 eV/Å respectively, and the energy cutoff of plane wave was 450 eV. A Γ-centered mesh of 4*1*1 is used for the Brillouin zone sampling in relaxing the original and adsorption structures of IrCoO-x slabs. As for the electronic structure analysis, all the single-point calculations are conducted with a Γ-centered mesh of 4*1*1. With a pH and an external potential of 0, the Gibbs free-energy change (ΔG) of the adsorption systems are calculated with VASPKIT[4], which includes the contribution of the electronic energy (ΔE), zero-point energy (ΔZPE), and entropy (ΔS).

$$\Delta G = \Delta E + \Delta ZPE - T\Delta S \#(9)$$

where T represents the temperature, and is set to 298 K.

Adsorbate Evolution Mechanism pathway, namely:

$$*H2O-*+H2O \rightarrow *H2O-*OH + (H++e-) \text{ (Step1)}$$

$$*H_2O-*OH \rightarrow *H_2O-*O + (H^+ + e^-) \text{ (Step2)}$$

$$*H_2O-*O + H_2O \rightarrow *H_2O-*OOH + (H^+ + e^-) \text{ (Step3)}$$

$$*H_2O-*OOH \rightarrow *H_2O-* + O_2 + (H^+ + e^-) \text{ (Step4)}$$

Dual-site synergy mechanism pathway, namely:

$$*H_2O-*+H_2O \rightarrow *H_2O-*OH + (H^+ + e^-) \text{ (Step1.1)}$$

$$*H_2O-*OH \rightarrow *H_2O-*O + (H^+ + e^-) \text{ (Step1.2)}$$

$$*H_2O-*O \rightarrow *OH-*O + (H^+ + e^-) \text{ (Step1.3)}$$

$$*OH-*O + H_2O \rightarrow *H_2O-*OOH \text{ (Step1.4)}$$

$$*H_2O-*OOH \rightarrow *H_2O-* + O_2 + (H^+ + e^-) \text{ (Step1.5)}$$

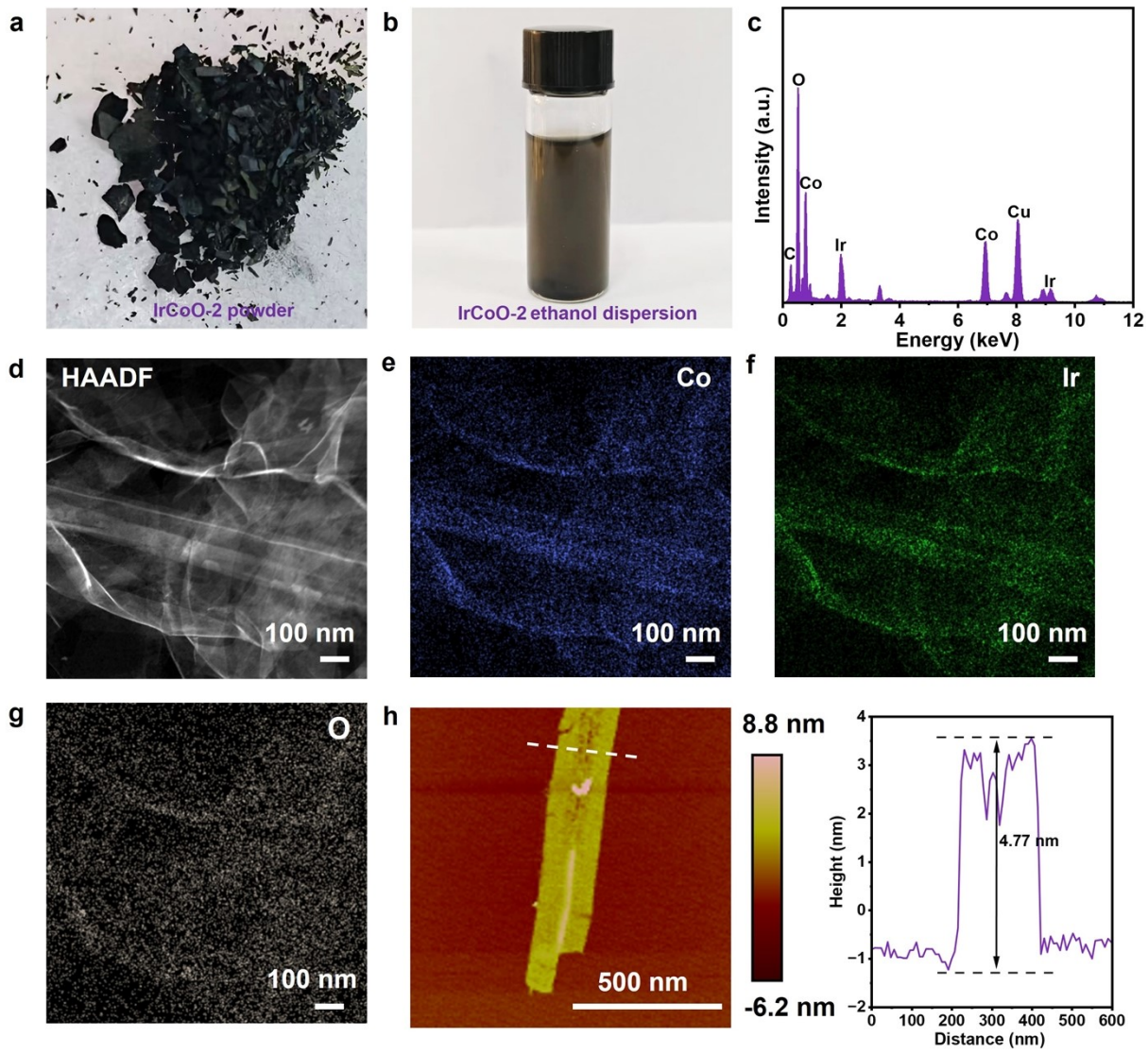

Figure S1. (a) The digital images of the IrCoO-2 powder and (b) its ethanol dispersion in a cuvette. (c) EDS energy spectrum of IrCoO-2. The HAADF-STEM and EDS elemental mapping images of (e) Co, (f) Ir and (g) O in IrCoO-2. (h) AFM images and corresponding height profiles of IrCoO-2.

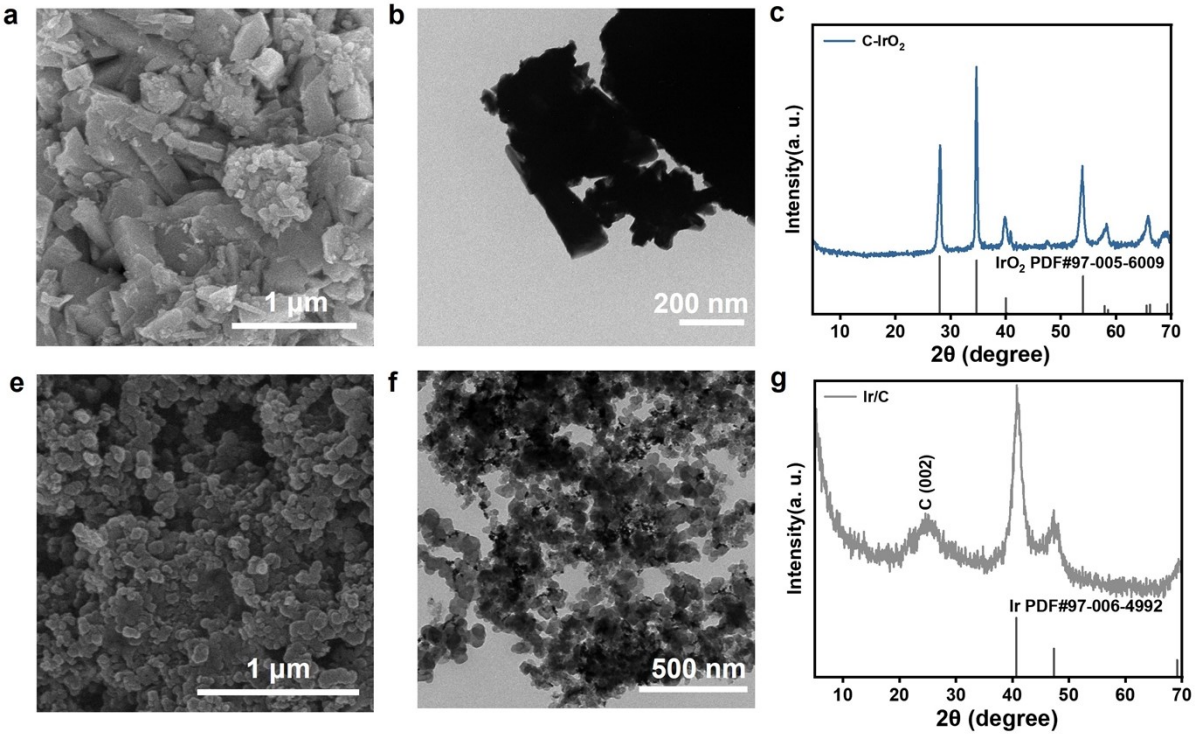

252

253 **Figure S2.** (a) SEM image and (b) TEM image of C-IrO_2. (c) XRD pattern of C-IrO_2. (e) SEM image and (f)

254 TEM image of Ir/C. (g) XRD pattern of Ir/C.

255

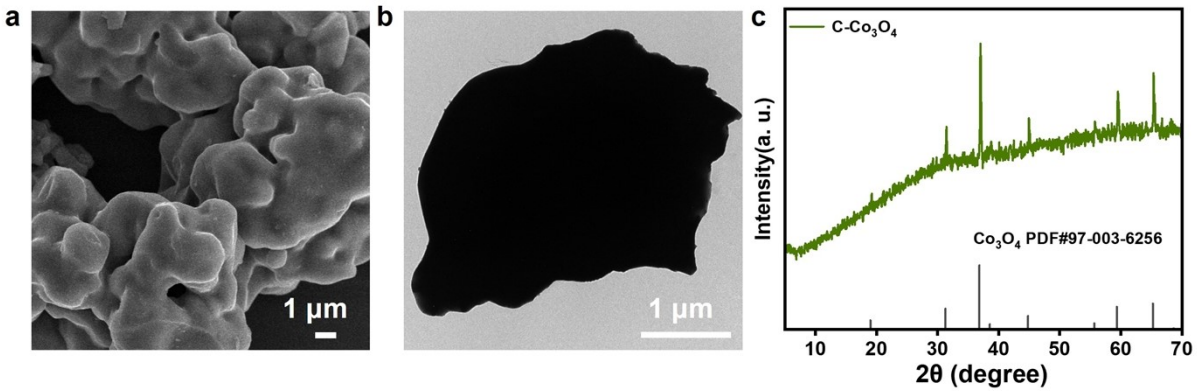

256

257 **Figure S3.** (a) SEM image and (b) TEM image of C-Co_3O_4. (c) XRD pattern of C-Co_3O_4.

258

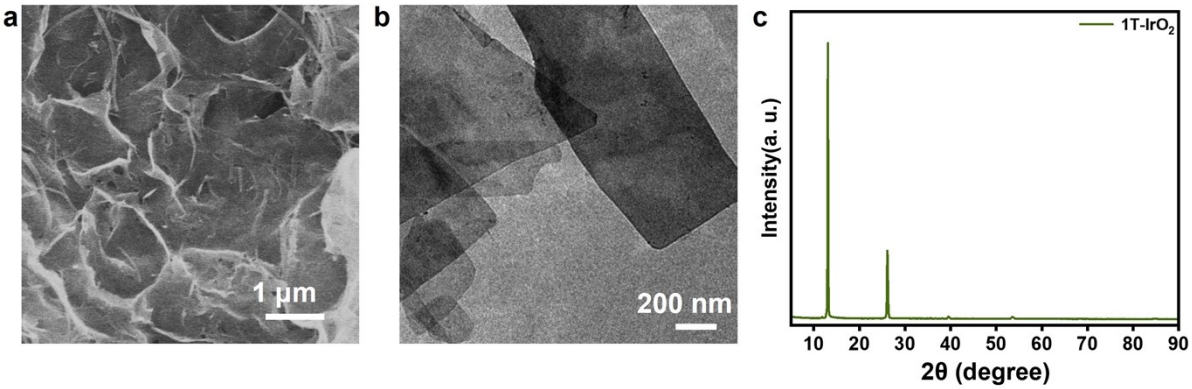

259

260 **Figure S4.** (a) SEM and (b) TEM images of 1T-IrO_2. (c) XRD pattern of 1T-IrO_2.

261

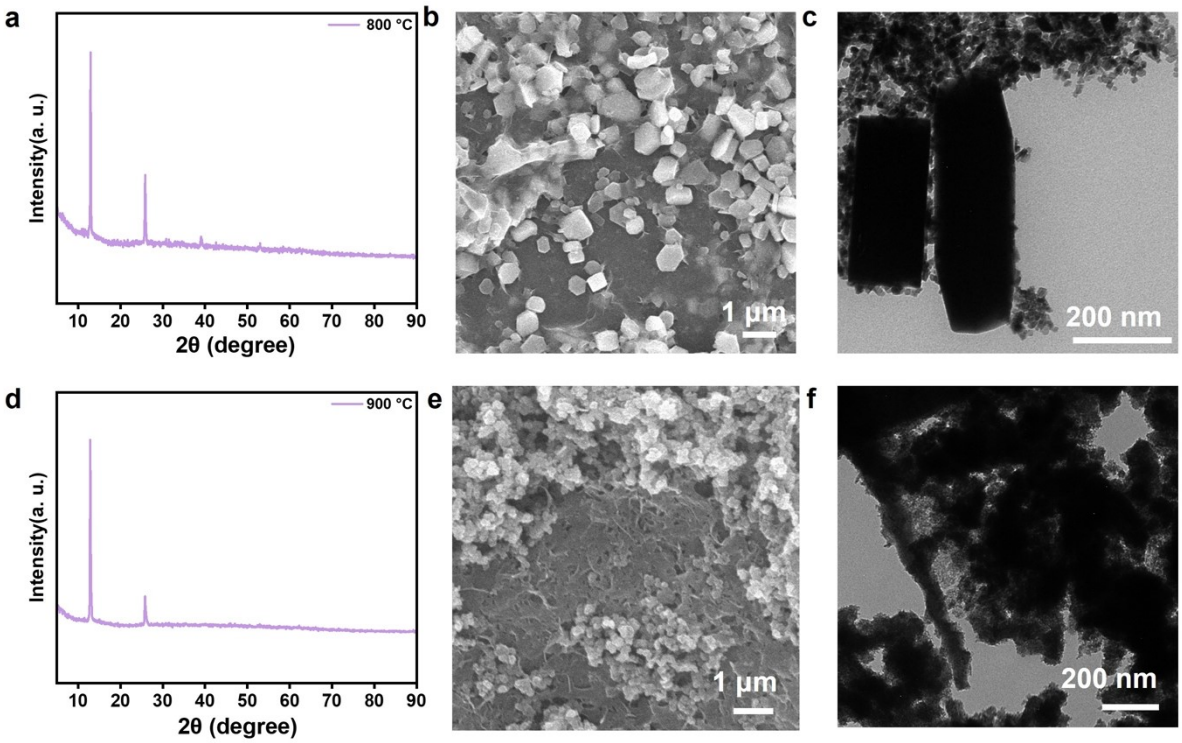

Figure S5. (a) XRD pattern, (b) SEM image and (c) TEM image of sample annealed at 800 ℃. (d) XRD pattern, (e) SEM image and (f) TEM image of sample annealed at 900 ℃.

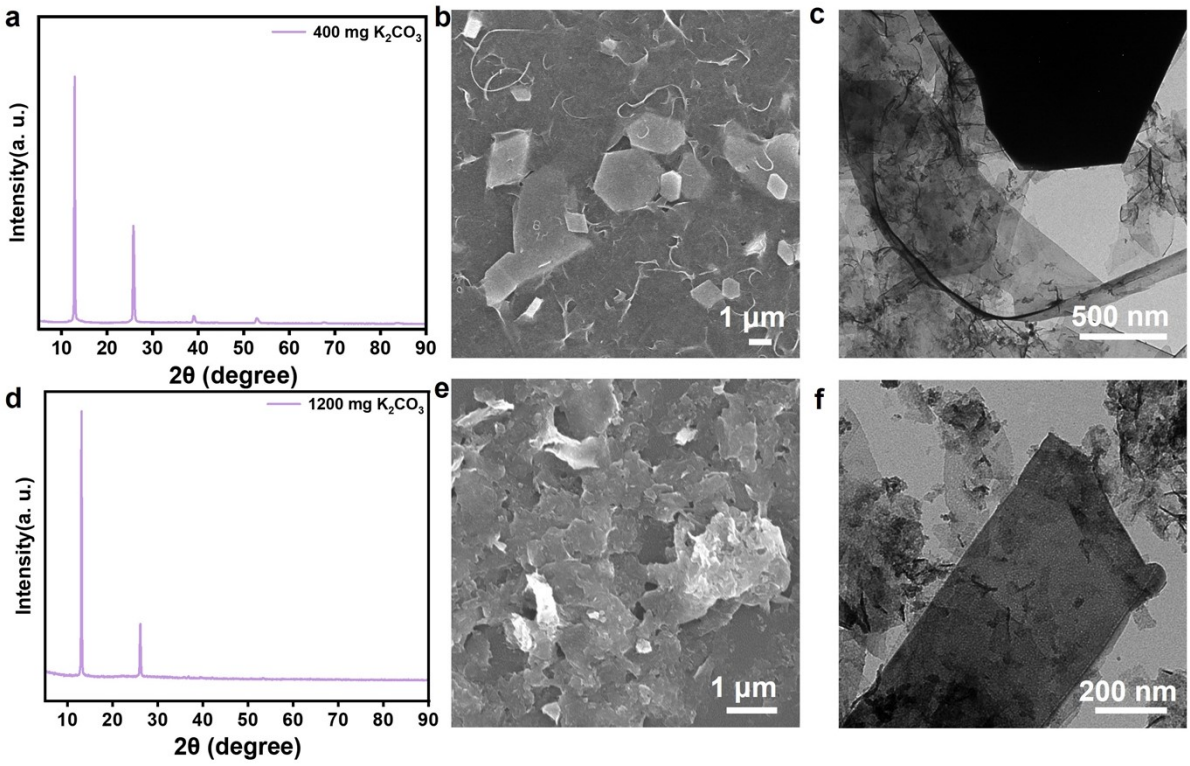

Figure S6. (a) XRD pattern, (b) SEM image and (c) TEM image of sample using relatively small amount of only 400 mg K_2CO_3 as the raw material. (d) XRD pattern, (e) SEM image and (f) TEM image of sample using excess K_2CO_3 reached 1200 mg as the raw material.

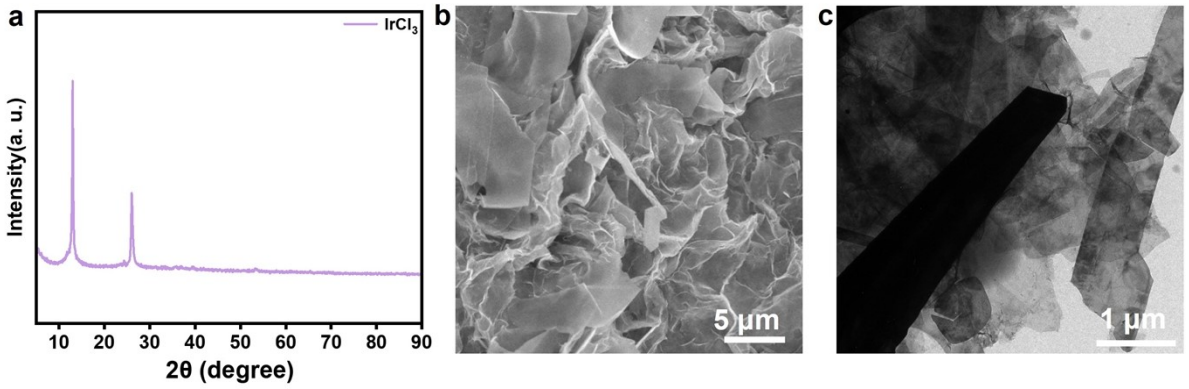

271

272 **Figure S7.** (a) XRD pattern, (b) SEM image and (c) TEM image of sample using $IrCl_3$ as the raw material.

273

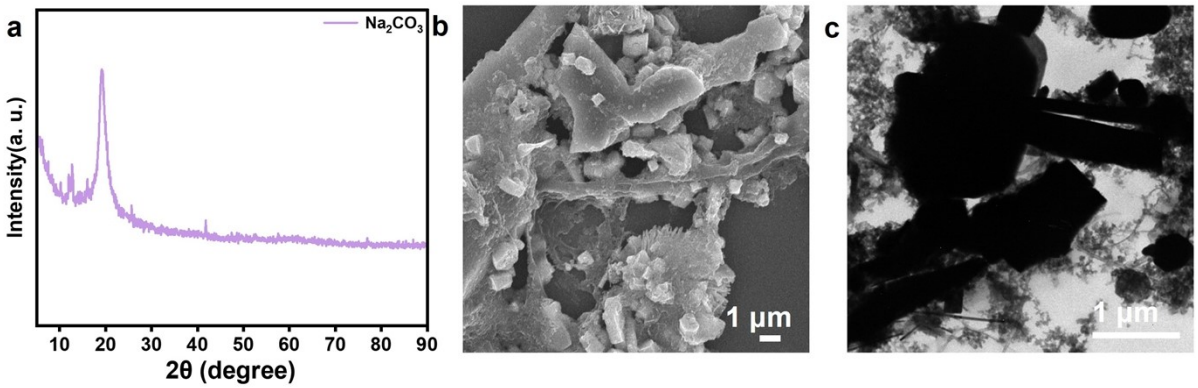

Figure S8. (a) XRD pattern, (b) SEM image and (c) TEM image of sample using Na_2CO_3 as the raw material.

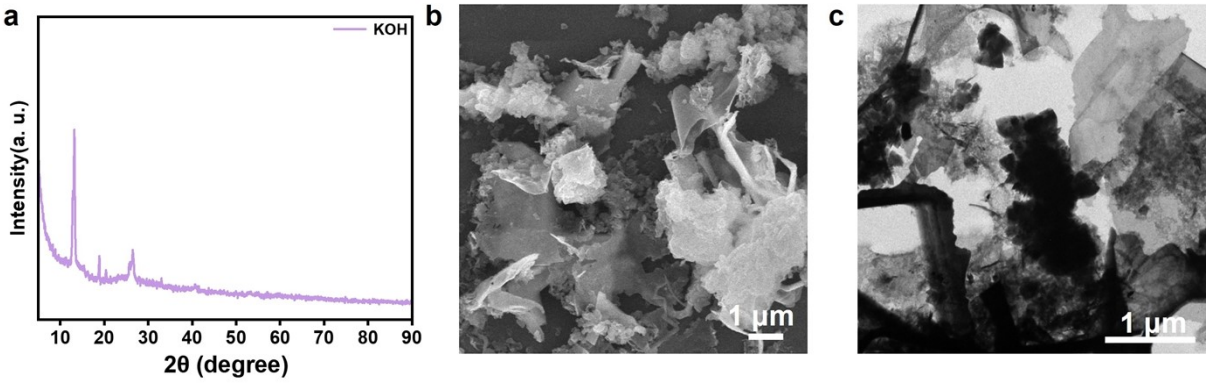

277

278 **Figure S9.** (a) XRD pattern, (b) SEM image and (c) TEM image of sample using KOH as the raw material.

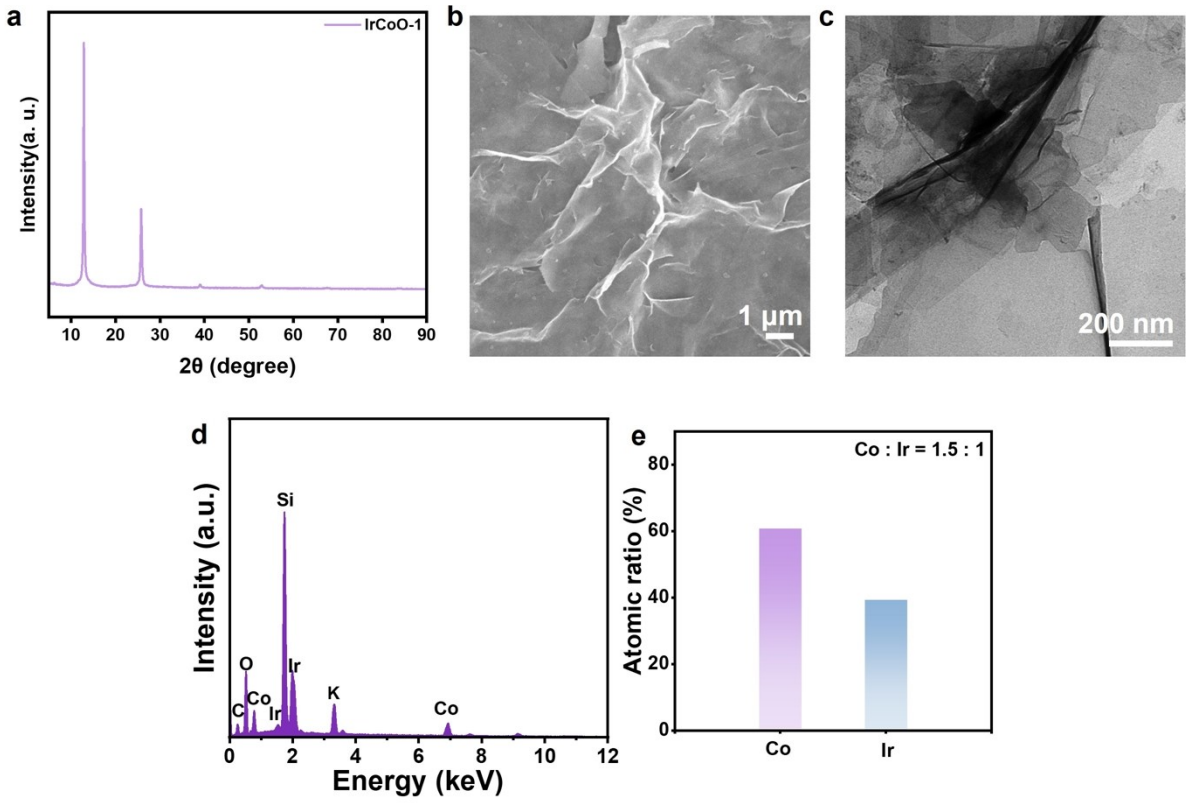

280

281 **Figure S10.** (a) XRD pattern of IrCoO-1. (b) SEM image of IrCoO-1. (c) TEM image of IrCoO-1. (d) EDS

282 image of IrCoO-1. (e) EDS analysis of IrCoO-1, where the ratio of Co to Ir is 1.5 : 1.

283

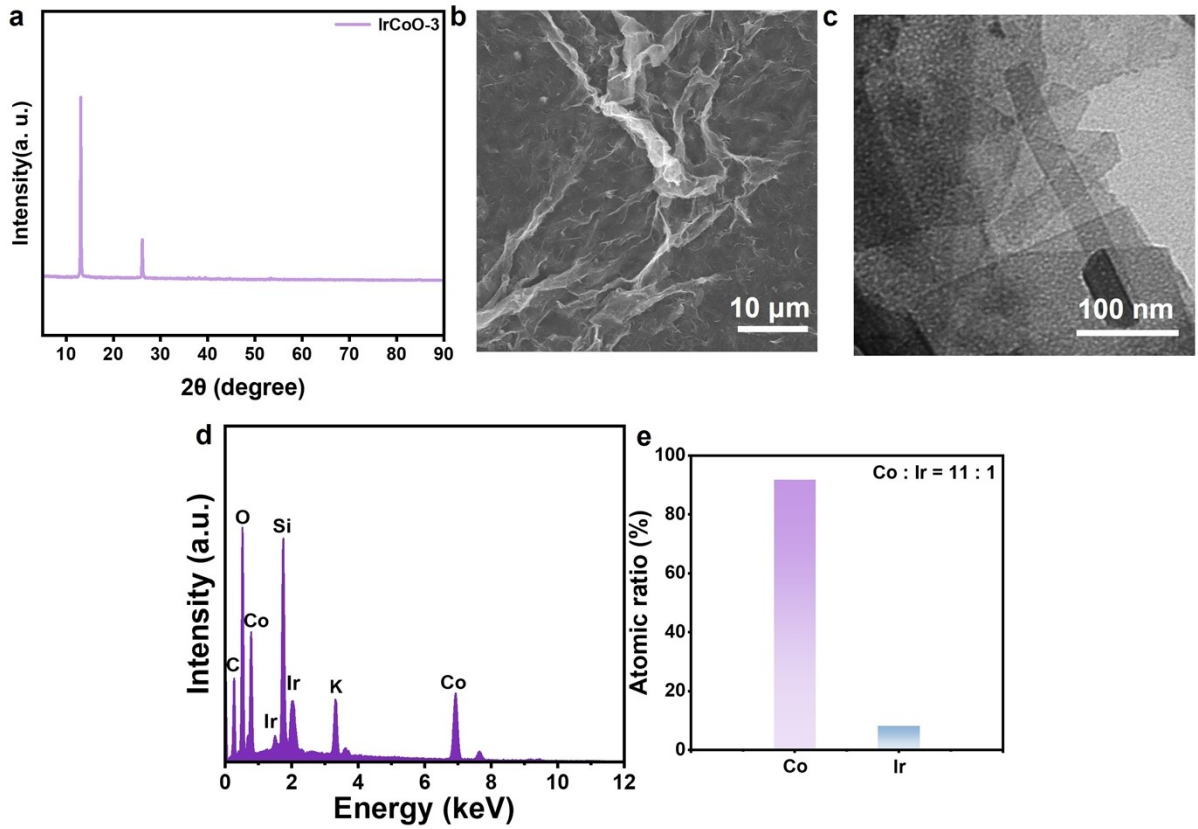

284

285 **Figure S11.** (a) XRD pattern of IrCoO-3. (b) SEM image of IrCoO-3. (c) TEM image of IrCoO-3. (d) EDS

286 image of IrCoO-3. (e) EDS analysis of IrCoO-3, where the ratio of Co to Ir is 11 : 1.

287

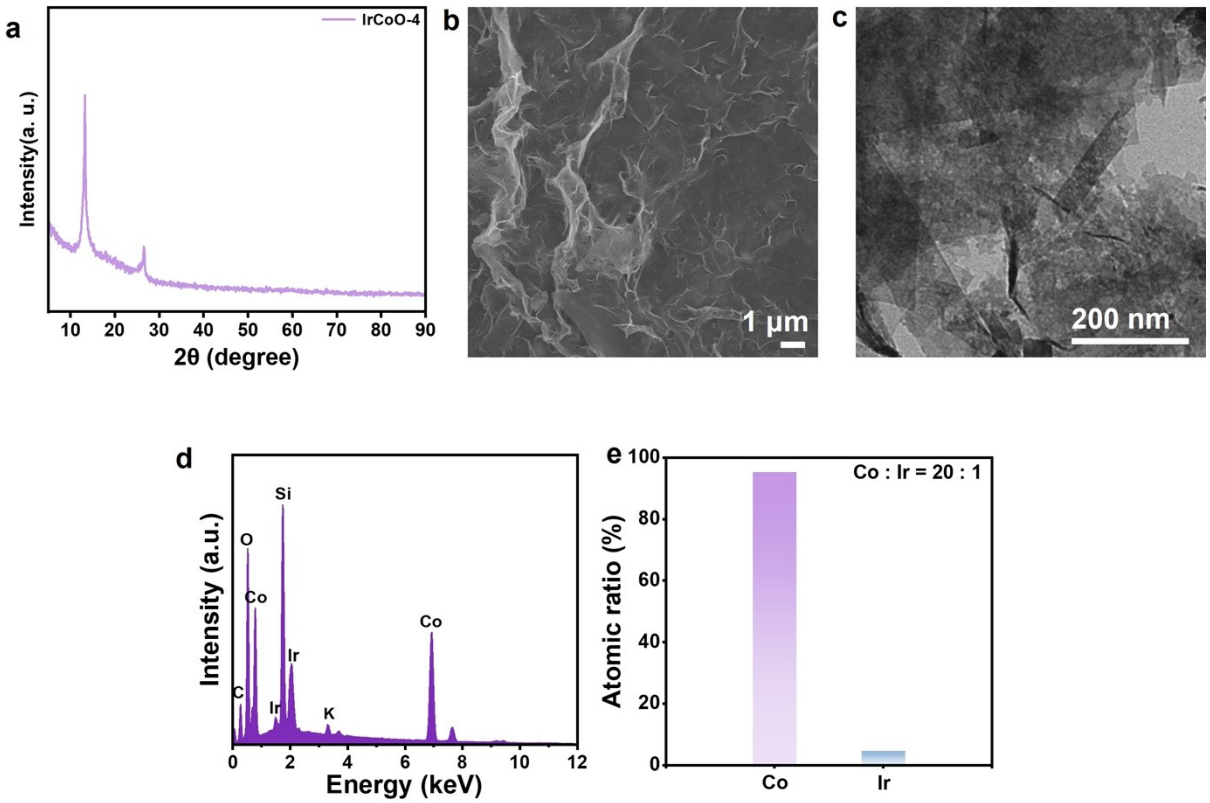

288

289 **Figure S12.** (a) XRD pattern of IrCoO-4. (b) SEM image of IrCoO-4. (c) TEM image of IrCoO-4. (d) EDS

290 image of IrCoO-4. (e) EDS analysis of IrCoO-4, where the ratio of Co to Ir is 20 : 1.

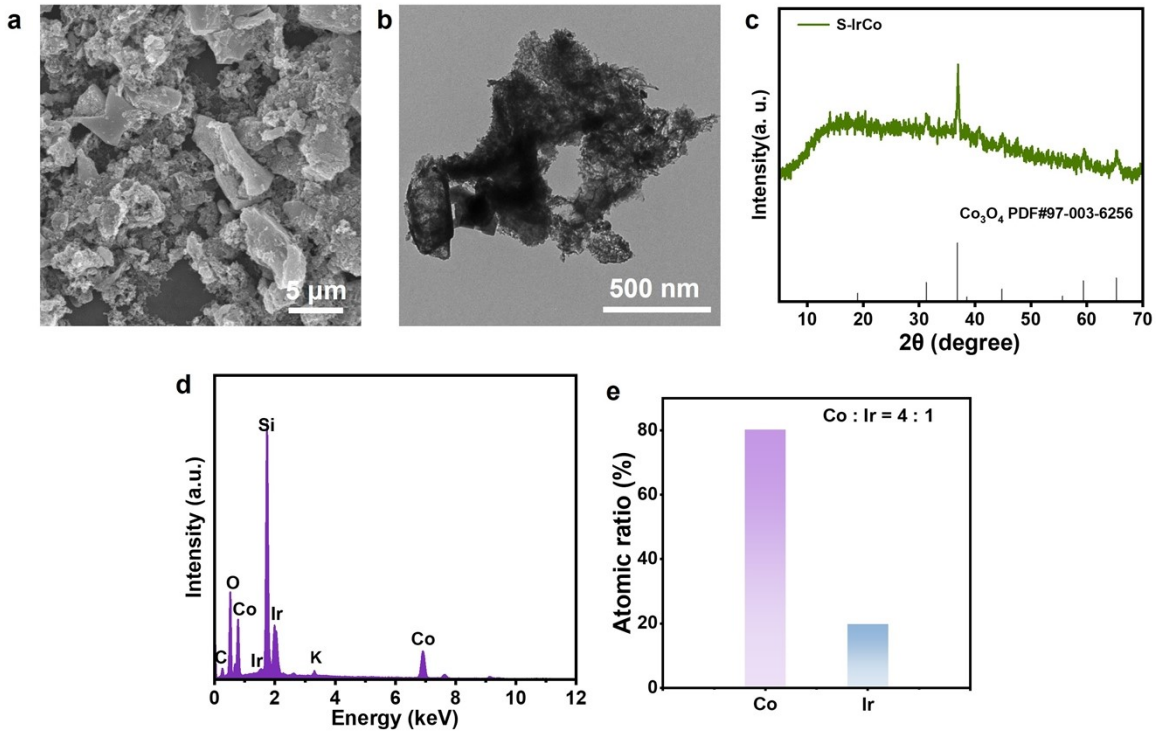

Figure S13. (a) SEM image of IrCoONPS. (b) TEM image of IrCoONPS. (c) XRD pattern of IrCoONPS. (d) EDS image of IrCoONPS. (e) EDS analysis of IrCoONPS, where the ratio of Co to Ir is 4 : 1.

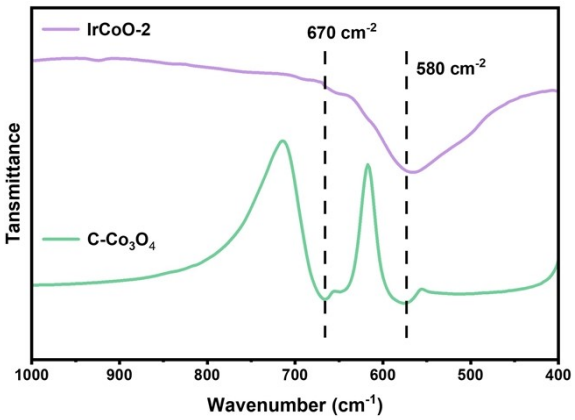

296

297 **Figure S14.** The IR spectrum of IrCoO-2 and C-Co_3O_4.

298

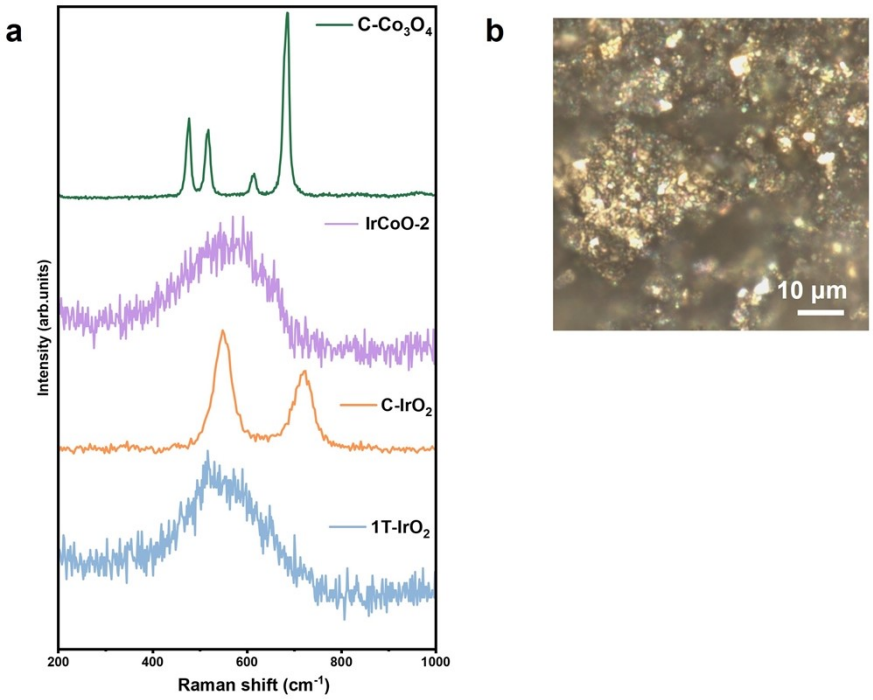

299

300 **Figure S15.** (a) Raman spectra of C-Co_3O_4, IrCoO-2 C-IrO_2 and 1T-IrO_2. (b) Raman image of IrCoO-2.

301

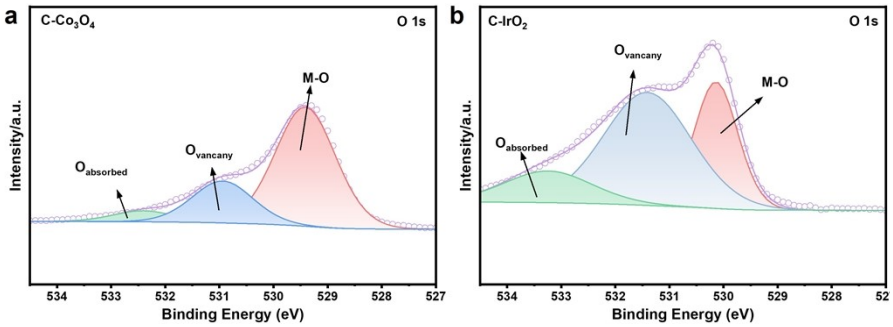

302

303 **Figure S16.** (a) O 1s XPS spectra of C-Co_3O_4. (b) O 1s XPS spectra of C-IrO_2.

304

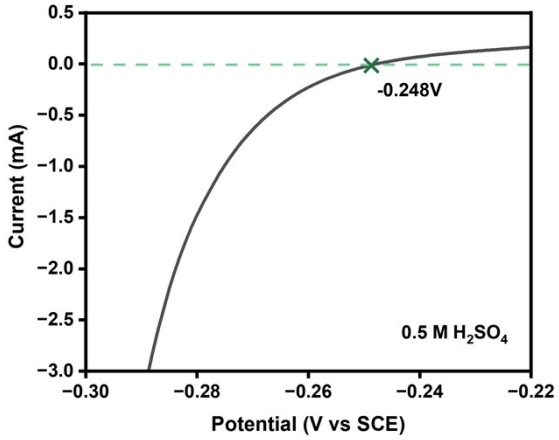

Figure S17. Potential calibration of the saturated calomel electrode in 0.5 M H_2SO_4 electrolyte. The calibration was performed in the high purity hydrogen-saturated electrolyte. Two Pt electrodes were used as the working and counter electrodes. Scan rate: 1 mV s^{-1}.

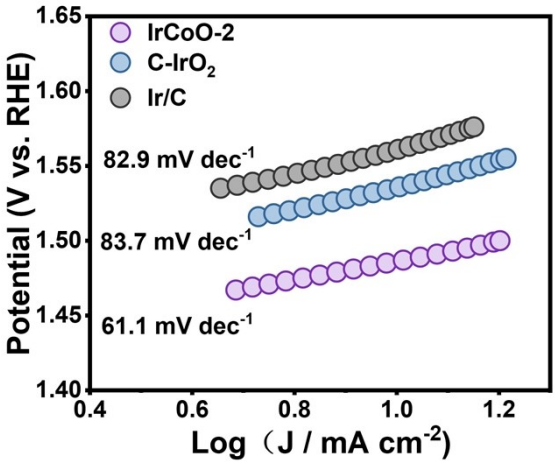

311

312 **Figure S18.** Tafel plots and corresponding Tafel slopes of IrCoO-2, C-IrO_2 and Ir/C.

313

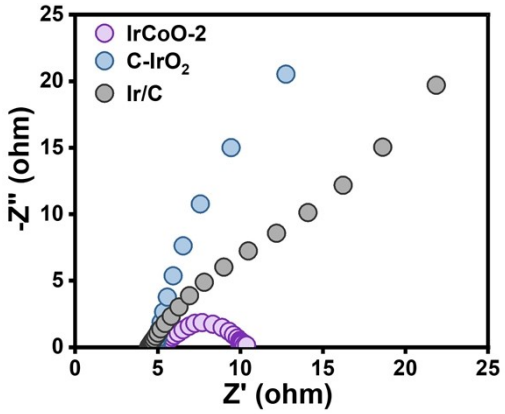

Figure S19. Nyquist diagrams of IrCoO-2, C-$IrO_2$and Ir/C. The EIS curves for IrCoO-2, C-IrO_2, and Ir/C at corresponding overpotentials for a current density of 10 mA cm^{-2} are presented respectively for OER in 0.5 M H_2SO_4.

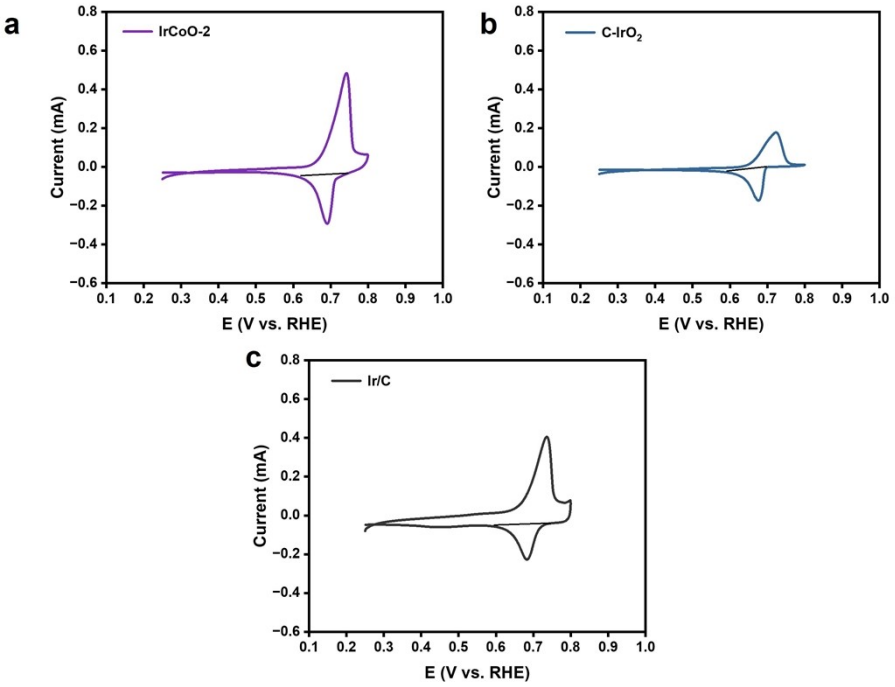

Figure S20. UPD method used to determine the ECSA. CV curves of (a) IrCoO-2, (b) C-IrO_2 and (c) Ir/C in 0.1 M $HClO_4$ containing 1.0 mM mercury nitrate. The scanning rate was 10 mV s^{-1}.

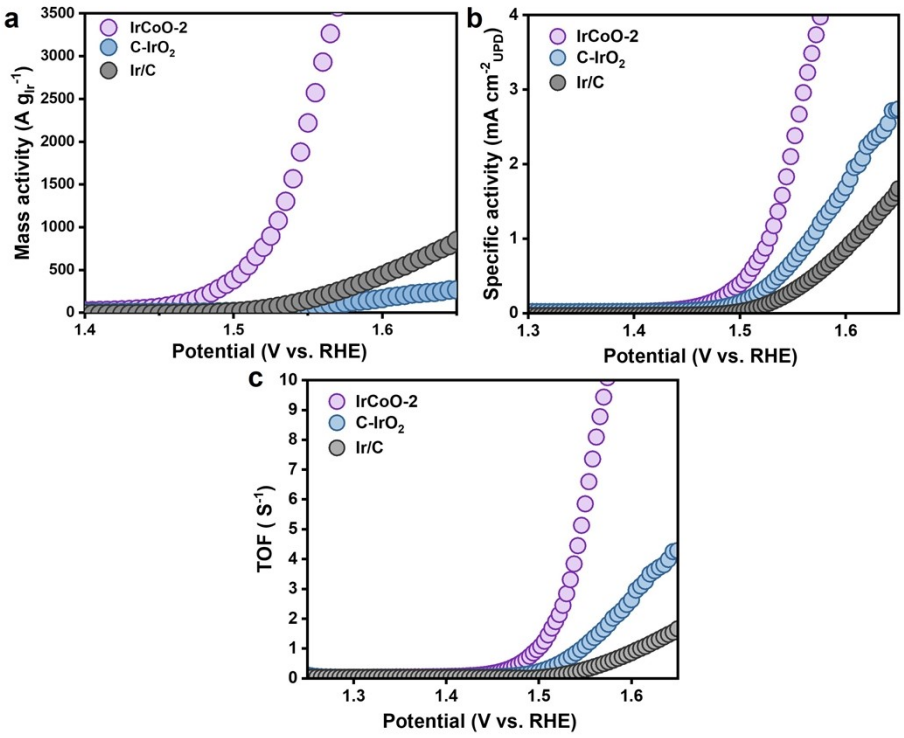

323

324 **Figure S21.** (a) Mass activity, (b) SA and (c) TOF of IrCoO-2, C-IrO_2 and Ir/C under different voltage

325 changes.

326

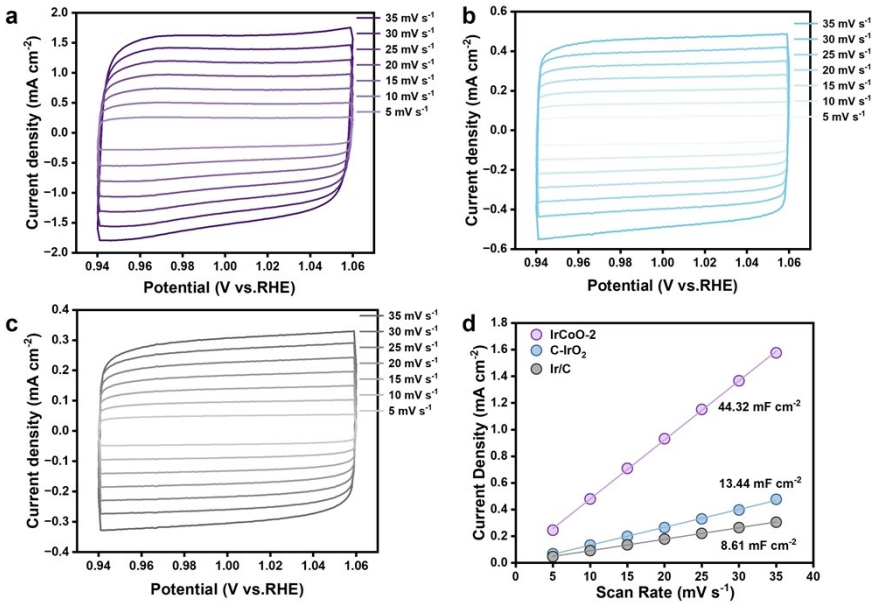

327

328 **Figure S22.** CV curves of (a) IrCoO-2, (b) C-IrO_2 and (c) Ir/C with different scan rates in a potential region

329 of 0.94 to 1.06 V *vs.* RHE in 0.5 M H_2SO_4. (f) The corresponding C_{dl} plots of IrCoO-2, C-IrO_2 and Ir/C.

330

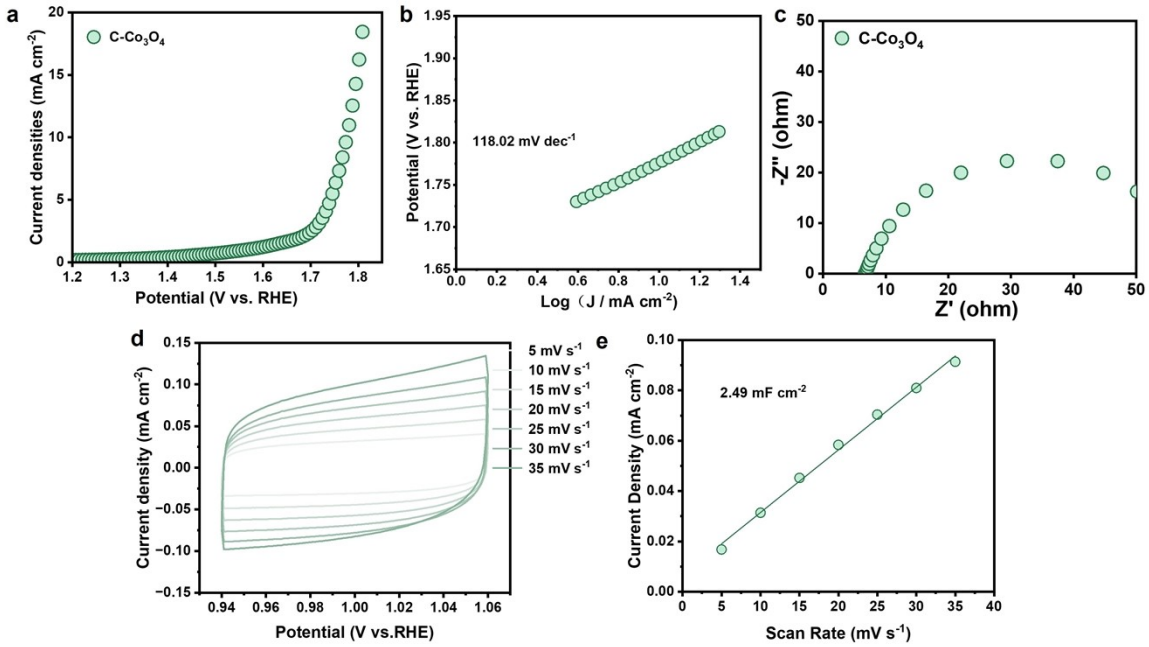

331

332 **Figure S23.** (a) Polarization curves of C-Co_3O_4 in O_2-saturated 0.5 M H_2SO_4 electrolyte with *i*R-correction,

333 where C-Co_3O_4 deliver an overpotential of 549 mV to achieve the current density of 10 mA cm^{-2}. (b) Tafel

334 plots of C-Co_3O_4. (c) Nyquist plot of C-Co_3O_4. (d) CV curve of C-Co_3O_4 with different scan rates in a

335 potential region of 0.94 to 1.06 V *vs.* RHE in 0.5 M H_2SO_4. (c) The corresponding C_{dl} plots of C-Co_3O_4.

336

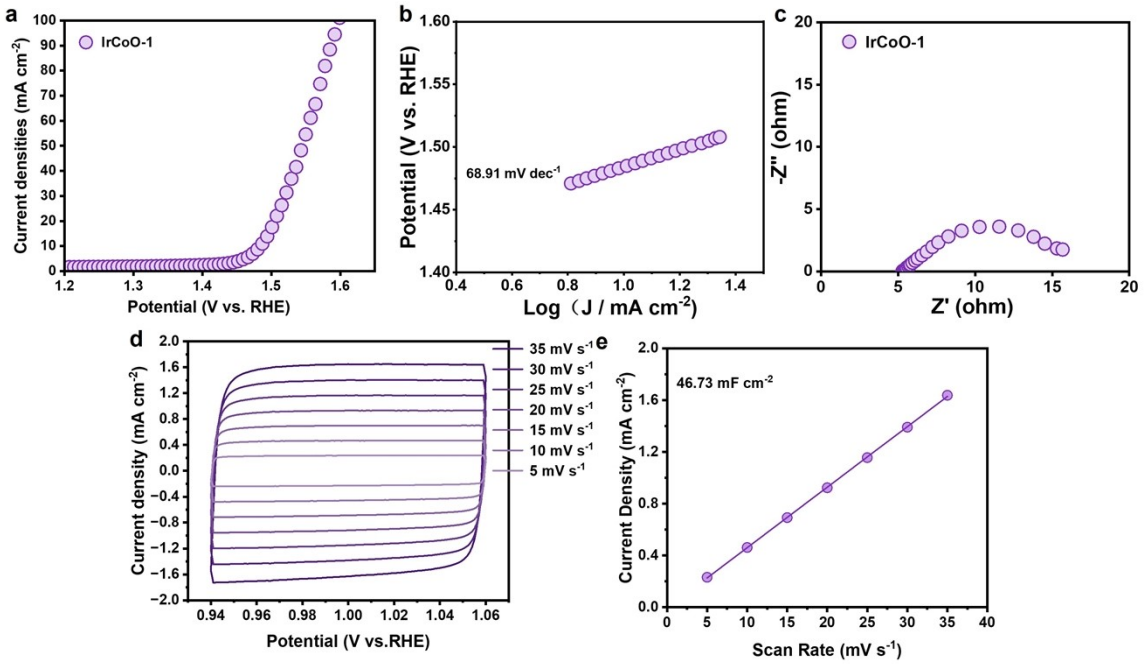

337

338 **Figure S24.** (a) Polarization curves of IrCoO-1 in O_2-saturated 0.5 M H_2SO_4 electrolyte with *i*R-correction,

339 where IrCoO-1 deliver an overpotential of 254 mV to achieve the current density of 10 mA cm^{-2}. (b) Tafel

340 plots of IrCoO-1. (c) Nyquist plot of IrCoO-1. (d) CV curve of IrCoO-1 with different scan rates in a

341 potential region of 0.94 to 1.06 V *vs.* RHE in 0.5 M H_2SO_4. (c) The corresponding C_{dl} plots of IrCoO-1.

342

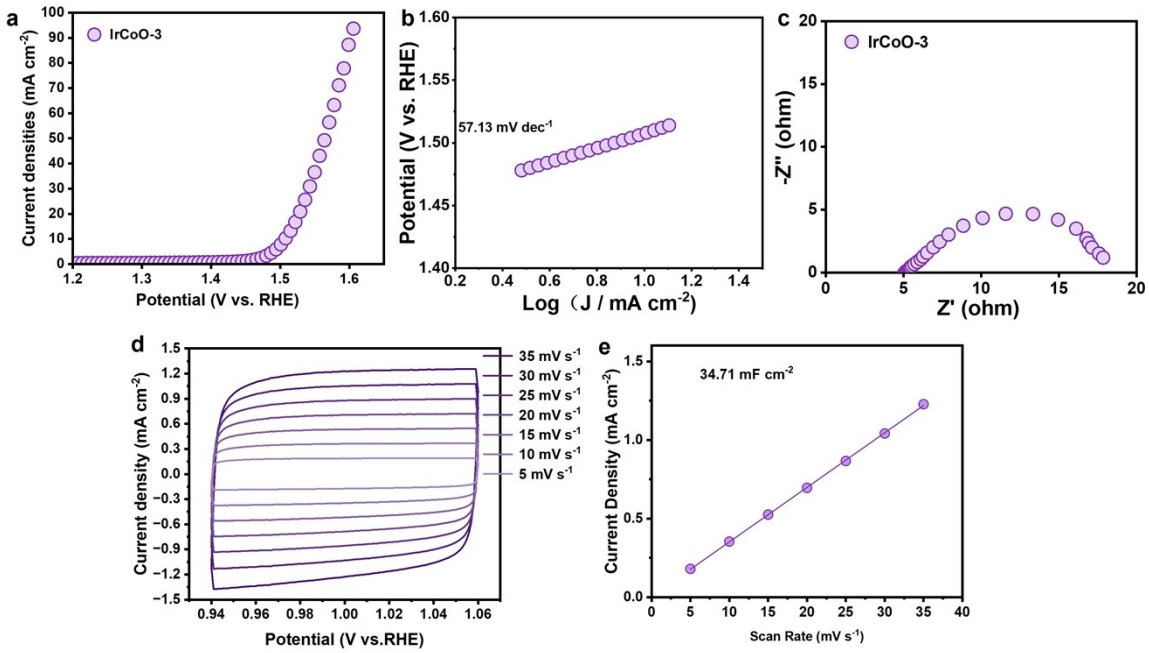

343

344 **Figure S25.** (a) Polarization curves of IrCoO-3 in O_2-saturated 0.5 M H_2SO_4 electrolyte with *i*R-correction,

345 where IrCoO-3 deliver an overpotential of 278 mV to achieve the current density of 10 mA cm^{-2}. (b) Tafel

346 plots of IrCoO-3. (c) Nyquist plot of IrCoO-3. (d) CV curve of IrCoO-3 with different scan rates in a

347 potential region of 0.94 to 1.06 V *vs.* RHE in 0.5 M H_2SO_4. (c) The corresponding C_{dl} plots of IrCoO-3.

348

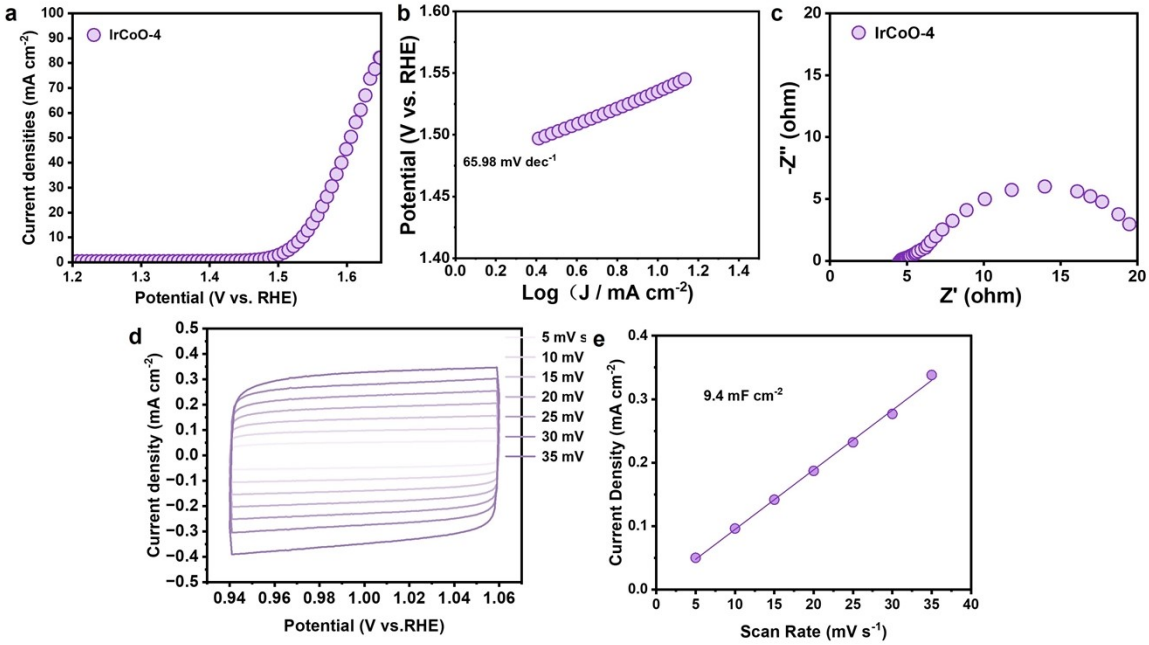

349

350 **Figure S26.** (a) Polarization curves of IrCoO-4 in O_2-saturated 0.5 M H_2SO_4 electrolyte with *i*R-correction,
351 where IrCoO-4 deliver an overpotential of 305 mV to achieve the current density of 10 mA cm^{-2}. (b) Tafel
352 plots of IrCoO-4. (c) Nyquist plot of IrCoO-4. (d) CV curve of IrCoO-4 with different scan rates in a
353 potential region of 0.94 to 1.06 V *vs.* RHE in 0.5 M H_2SO_4. (c) The corresponding C_{dl} plots of IrCoO-4.

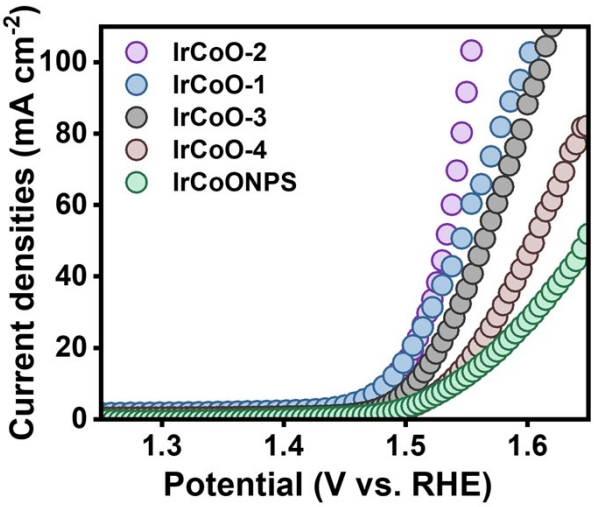

355

356 **Figure S27.** LSV curves of the samples of IrCoO-2, IrCoO-1, IrCoO-3, IrCoO-4 and IrCoONPS.
357

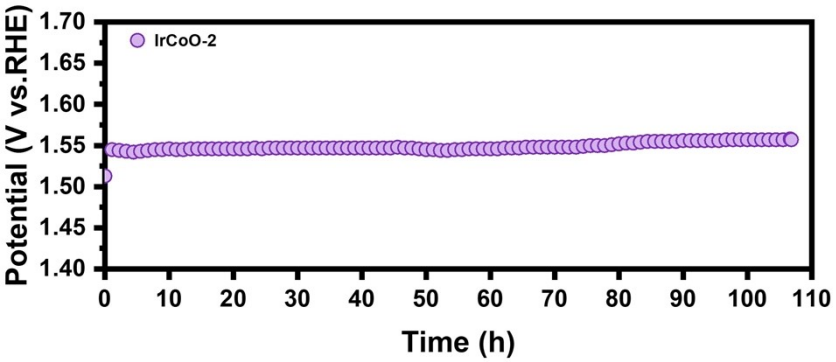

358

359 **Figure S28.** Chronopotentiometry test of IrCoO-2 at the current density of 10 mA cm^{-2} in 0.5 M H_2SO_4.

360

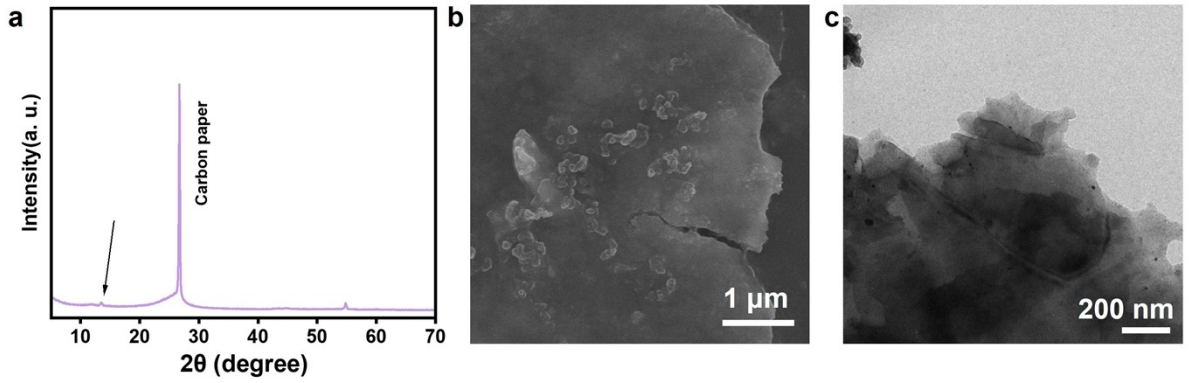

361

362 **Figure S29.** (a) XRD pattern, (b) SEM image and (c) TEM image of IrCoO-2 after 106 hours stability test.

363

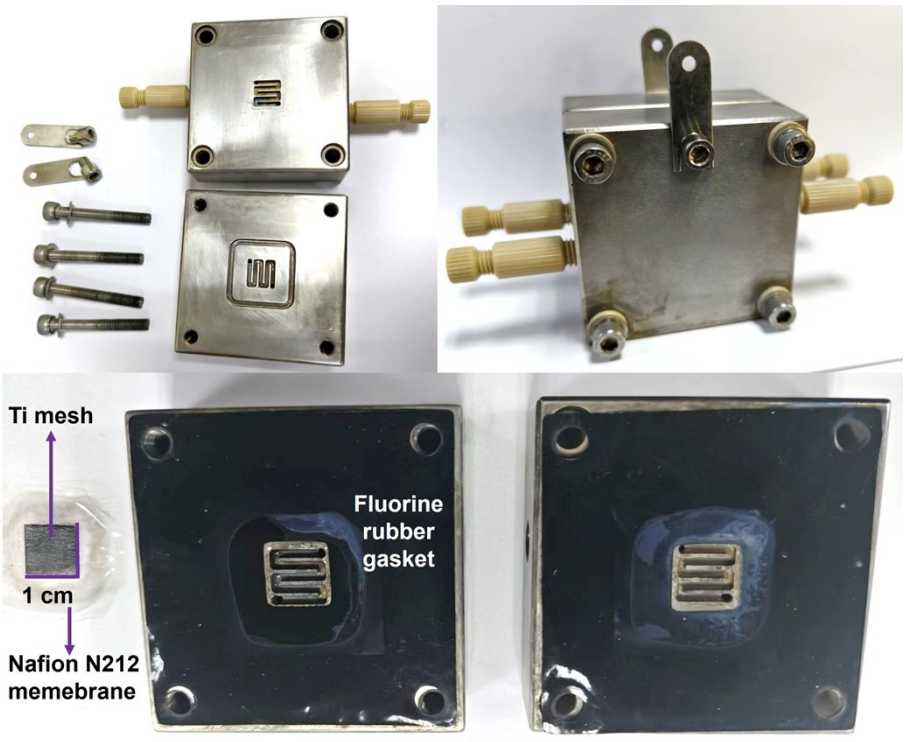

364

365 **Figure S30.** Actual device diagram of PEMWE. The area of Ti mesh is 1×1 cm^2.

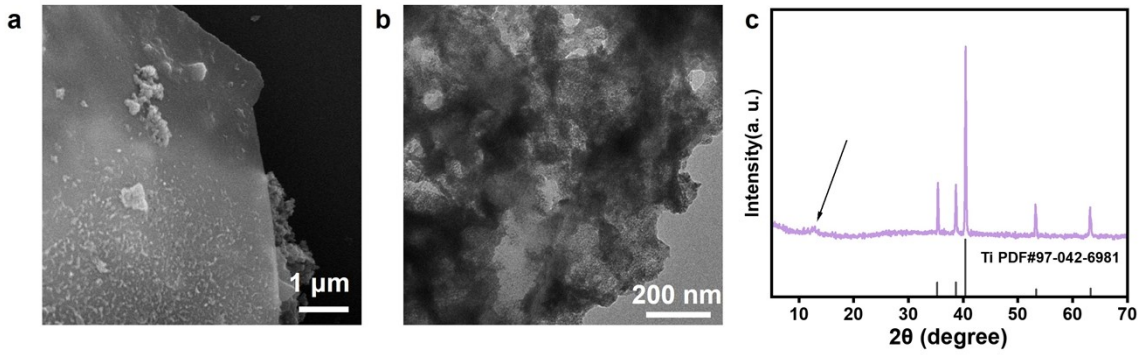

Figure S31. (a) SEM image, (b) TEM image and (c) XRD pattern of IrCoO-2 after 600 hours stability test in PEM device.

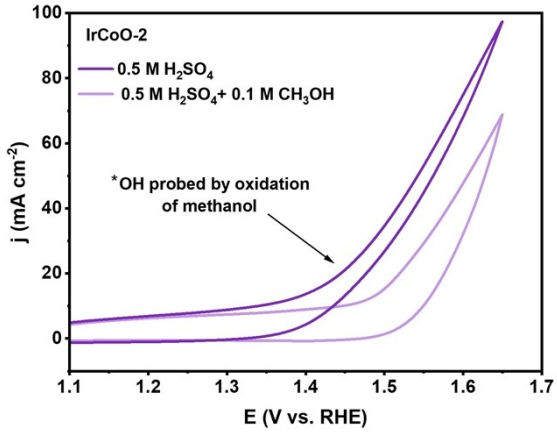

Figure S32. CV curves of IrCoO-2 recorded with and without 0.1 M methanol at the scan rate of 50 mV s^{-1}.

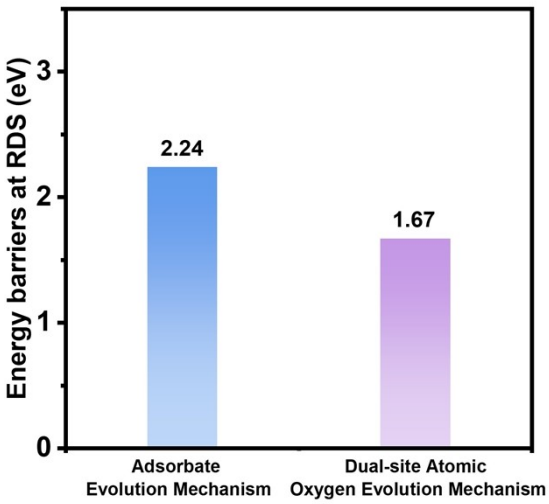

375

376 **Figure S33.** Comparisons of the energy barriers at the AEM and dual-site atomic oxygen evolution

377 mechanism of IrCoO-2.

378

Table S1. The quantity of raw materials input, the iridium-to-cobalt ratio in the catalyst and the catalyst nomenclature.

The usage amount of $C_{10}H_{14}IrO_4$ (mg)	The usage amount of $C_{10}H_{14}CoO_4$ (mg)	The usage amount of K_2CO_3 (g)	The atomic ratio of Ir to Co	Catalyst name
5	10	0.32	1 : 1.5	IrCoO-1
5	25	0.8	1 : 4	IrCoO-2
5	75	2.4	1 : 11	IrCoO-3
5	125	4	1 : 20	IrCoO-4

Table S2. Overpotential and Tafel slope of IrCoO-1, IrCoO-2, IrCoO-3, IrCoO-4, IrCoONPS, C-IrO_2 and Ir/C in 0.5 M H_2SO_4.

Catalyst	Overpotential @ 10 mA cm^{-2} (mV)	Tafel slope (mV dec^{-1})
IrCoO-1	254	68.9
IrCoO-2	256	61.1
IrCoO-3	278	57.1
IrCoO-4	305	66.0
IrCoONPS	311	88.9
C-IrO_2	306	83.7
Ir/C	331	82.9

Table S3. Comparison of C_{dl}, mass activity, UPD based ECSA and TOF among the catalysts in acidic OER.

Catalyst	C_{dl} (mF cm^{-2})	Hg UPD Area (m^2 g^{-1})	Mass activity @ 1.53 V vs. RHE (A g$^{-1}_{Ir}$)	Specific activity @ 1.53 V vs. RHE (mA cm$^{-2}_{UPD}$)	TOF @ 1.53 V vs. RHE (s^{-1})
IrCoO-2	44.32	32.48	1076.8	1.08	2.84
C-IrO_2	13.44	8.31	39.5	0.40	0.63
Ir/C	8.61	10.04	74.4	0.15	0.15

Table S4. The comparison of the OER performances (overpotential and mass activity) of IrCoO-2 and various reported catalysts.

Catalysts	Electrolyte	Overpotential (mV)	Mass activity @ 1.53 V vs. RHE (A g^{-1}_{Ir})	Reference
IrCoO-2	0.5 M H_2SO_4	256	1076.8	This work
C-IrO_2	0.5 M H_2SO_4	305	41.7	This work
Ir/C	0.5 M H_2SO_4	332	68.8	This work
IrO_2@TaB_2 (16%)	0.1 M $HClO_4$	288	345	5
IrW-W_2B	0.5 M H_2SO_4	291	518	6
IrO_x·nH2O	0.1 M $HClO_4$	283	200	7
Ir_1O_6–Co_3O_4	0.1 M $HClO_4$	253	519	8
IrO_2/OH-ZrP	0.1 M $HClO_4$	269	798	9
Li–IrO_x	0.5 M H_2SO_4	300	100 @1.52 V	10

IrO_2/S-450	0.5 M H_2SO_4	276	133.27	11
KIr_4O8	0.5 M H_2SO_4	266	109.6	12
IrO_2@TaOx@TaB	0.1 M $HClO_4$	279	225	13
IrY	0.5 M H_2SO_4	255	96.3	14
D-$IrTe_2$ HNSs	0.5 M H_2SO_4	298	213.8 @1.50 V	15
RuO_2/$(Co,Mn)_3O_4$/CC	0.5 M H_2SO_4	270	366.5	16

389

Reference

1 G. Kresse and J. Furthmüller, Phys. Rev. B, 1996, **54**, 11169–11186.
2 P. E. Blöchl, Phys. Rev. B, 1994, **50**, 17953–17979.
3 J. P. Perdew, K. Burke and M. Ernzerhof, Phys. Rev. Lett., 1996, **77**, 3865–3868.
4 V. Wang, N. Xu, J.-C. Liu, G. Tang and W.-T. Geng, Comput. Phys. Commun., 2021, **267**, 108033.
5 Y. Wang, M. Zhang, Z. Kang, L. Shi, Y. Shen, B. Tian, Y. Zou, H. Chen and X. Zou, Nat. Commun., 2023, **14**, 5119.
6 R. Li, H. Wang, F. Hu, K. C. Chan, X. Liu, Z. Lu, J. Wang, Z. Li, L. Zeng, Y. Li, X. Wu and Y. Xiong, Nat. Commun., 2021, **12**, 3540.
7 J. Xu, H. Jin, T. Lu, J. Li, Y. Liu, K. Davey, Y. Zheng and S.-Z. Qiao, Sci. Adv., 2023, **9**, eadh1718.
8 W. Li, J. Zhang, C. Yang, Z. Geng, X. Chen, Q. Liu, B. Wang and L. Wang, J. Am. Chem. Soc., 2025, **147**, 40697–40707.
9 W. Li, J. Lv, X. Chen, B. Wang and L. Wang, J. Am. Chem. Soc., 2025, **147**, 29505–29516.
10 J. Gao, C.-Q. Xu, S.-F. Hung, W. Liu, W. Cai, Z. Zeng, C. Jia, H. M. Chen, H. Xiao, J. Li, Y. Huang and B. Liu, J. Am. Chem. Soc., 2019, **141**, 3014–3023.
11 C. Yang, Y. Zhu, F. Zhang, L. Yao, Y. Chen, T. Lu, Q. Li, J. Li, G. Wang, Q. Cheng and H. Yang, Adv. Mater., 2025, **37**, 2507560.
12 Z. Li, X. Li, M. Wang, Q. Wang, P. Wei, S. Jana, Z. Liao, J. Yu, F. Lu, T. Liu and G. Wang, Adv. Mater., 2024, **36**, 2402643.
13 Y. Wang, Z. Zhao, X. Liang, X. Zhao, X. Wang, S. Jana, Y. A. Wu, Y. Zou, L. Li, H. Chen and X. Zou, Adv. Mater., 2024, **36**, 2407717.
14 X. Xiong, J. Tang, Y. Ji, W. Xue, H. Wang, C. Liu, H. Zeng, Y. Dai, H.-J. Peng, T. Zheng, C. Xia, X. Liu and Q. Jiang, Adv. Energy Mater., 2024, **14**, 2304479.
15 Y. Pi, Y. Xu, L. Li, T. Sun, B. Huang, L. Bu, Y. Ma, Z. Hu, C.-W. Pao and X. Huang, Adv. Funct. Mater., 2020, **30**, 2004375.
16 S. Niu, X.-P. Kong, S. Li, Y. Zhang, J. Wu, W. Zhao and P. Xu, Appl. Catal., B, 2021, **297**, 120442.